UNIVERSITY OF
GLOUCESTERSHIRE

This is a peer-reviewed, post-print (final draft post-refereeing) version of the following published document and is licensed under Creative Commons: Attribution-Noncommercial-No Derivative Works 4.0 license:

Mokhtari, Zahra, Amani-Beni, Majid, Asgarian, Ali, Russo, Alessio ORCID logoORCID: https://orcid.org/0000-0002-0073-7243, Qureshi, Salman and Karami, Ayoob (2023) Spatial prediction of the urban inter-annual land surface temperature variability: An integrated modeling approach in a rapidly urbanizing semi-arid region. Sustainable Cities and Society, 93. Art 104523. doi:10.1016/j.scs.2023.104523

Official URL: https://doi.org/10.1016/j.scs.2023.104523
DOI: http://dx.doi.org/10.1016/j.scs.2023.104523
EPrint URI: https://eprints.glos.ac.uk/id/eprint/12585

Disclaimer

The University of Gloucestershire has obtained warranties from all depositors as to their title in the material deposited and as to their right to deposit such material.

The University of Gloucestershire makes no representation or warranties of commercial utility, title, or fitness for a particular purpose or any other warranty, express or implied in respect of any material deposited.

The University of Gloucestershire makes no representation that the use of the materials will not infringe any patent, copyright, trademark or other property or proprietary rights.

The University of Gloucestershire accepts no liability for any infringement of intellectual property rights in any material deposited but will remove such material from public view pending investigation in the event of an allegation of any such infringement.

PLEASE SCROLL DOWN FOR TEXT.

Spatial prediction of the urban inter-annual land surface temperature variability: An integrated modeling approach in a rapidly urbanizing semi-arid region

Abstract

The inter-annual land surface temperature (LST) is a meteorological indicator of urban environments, affecting energy consumption and quality of life. In this study, the annual LST variability (ALSTV) of a rapidly urbanizing region in Iran including Karaj, Shahriar and Mohammad-Shahr cities and their surrounding suburbs was estimated using Landsat-8 images. Pixel-based image classification and object-based segmentation techniques were employed to extract built-up patches and spectrally homogeneous regions. Using the multiple regression analysis, the ALSTV of built-up patches was modeled as a function of their structure and the spatial characteristics of other land-use patches located in their respective segments (as neighborhood factors). A Cellular Automata model was utilized to simulate the expansion of built-up area up to 5% and, therefore, estimate their future ALSTV. The mean ALSTV was highest in urban areas (33.25± 7.41 °C), while the lowest mean value of 24.12± 3.24 °C was in green covers. The ALSTV of built-up patches were positively associated with their area and the percentage and size of neighborhood built-up patches, while negatively with the percentage of neighborhood green patches. To create a thermally comfortable landscape, additional green patch allocation and preventing excessive urban patch growth are required in all large built-up segments.

Keywords: Cellular Automata; Landscape metrics; Spatial pattern; Urban landscape planning; Karaj.

Introduction

Since the first decade of the 21st century, a progressive study in thermal remote sensing has brought out new research subjects associated with the thermal behavior of various land use/ land cover (LULC) classes from a single patch (Wang, Zhan, & Ouyang, 2017) to complex human-altered landscapes (Gao, Zhan, Yang, & Liu, 2020; Y. Liu, Peng, & Wang, 2018). These characteristics are all retrieved from various satellite images such as Landsat 8- thermal infrared sensor (TIRS) and Moderate Resolution Imaging Spectroradiometer (MODIS) thermal infrared data, which are known as Land Surface Temperature (LST) (Avdan & Jovanovska, 2016). With the growing availability of LST data in various spatio-temporal scales, LST has been recognized as a key variable in environmental studies ranging from crop water-stress detection (Gerhards et

al. 2019), water resources management (Kumar 2015), and geothermal activity of volcanoes (Muravyev 2018) to urban thermal comfort (Feng et al. 2020) and urban growth management (Rao et al. 2021; Lakra and Sharma 2019; Achmad et al. 2022). In human-altered landscapes, significant associations were also found between thermal characteristics of different LULC classes and other environmental processes such as Urban Heat Island (UHI) (Ren et al. 2021).

Nowadays, a large body of research has been done regarding the influence of LULC spatial patterns on LST (Azhdari, et al., 2018; Tang et al. 2018; H. Zhao et al. 2020). However, geographical conditions such as climate and topography were found to be important factors in determining the relationship between LST and LULC patterns. Moreover, patch interior characteristics and the cooling potential of LULCs such as vegetation (green) covers also determine how different LULC patterns affect LST at different times of the year (Sun et al. 2020; Allen et al. 2021). These varying conditions and factors highlight the necessity of forming innovative methodological frameworks to develop urban planning and management insights into the effect of different spatio-temporal LULC patterns on LST attributes in warm and cold periods. Besides the increasing technical performance of LULC classification and LST retrieval (Sekertekin and Bonafoni 2020), the utility of landscape metrics and spatial LULC change simulation models have been extensively employed as useful means to investigate the relationships between LULC patterns and LST variability. In the realm of LST studies, landscape metrics have been applied in numerous research in delineating the relationships between LULC patterns and LST (Tang et al. 2018; H. Zhao et al. 2020; Effati 2022).

Drawing from landscape ecology, the neighboring attributes are considered to be affective on LST in urban areas (Qiu & Jia, 2020). The edge effect as a neighboring characteristic provided a theoretical framework to investigate the ecological consequences of urban landscape modification

and fragmentation (Peng et al. 2022). Studies adopting this concept assume the spatial pattern of LULC, particularly urban patches, affects the neighboring areas at a certain distance or the entire landscape (Asgarian et al. 2015). Therefore, these findings demonstrate that the neighboring variables affects local LST. To explore the neighborhood effects on LST, in literature, several techniques have been adopted. For instance, Meng et al. (2022) employed the moving window method to explore the effect of neighboring characteristics on LST in Beijing, China. However, there is still no precise definition of what factors represent the neighborhood and how much LULC patches are affected by the neighbors due to the complexity of LULC relationships and interaction processes as well as the effect of climate at landscape levels.

Moreover, in the realm of LULC-LST relationship studies, there has been established a new paradigm concerning possible changes in future LULC classes on urban LST and thermal environments. In this case, Khan et al. (2022) predicted future LULC and LST changes in the Swabi District of Pakistan using an integrated weighted cellular automata (CA) model, finding that appropriate allocation of LULC classes might alleviate the creation of UHIs associated with urbanization and built-up areas. Rehman et al. (2022) analyzed a time-series LULC and its associated LST changes using a combination of remote sensing, statistical methods, and the spatial CA model. They found that urban area expansion is the primary cause of increased LST in urban areas. Bozorgi et al. (2018) developed a scenario-based approach to determine how different LULC changes affect future LST. A regional-scale study by Afrakhteh et al. (2016) revealed that the area of urban patches is a crucial factor that determines urban LST. They also built significant statistical urban area-LST relationships to model future urban LST in a rapidly growing region.

Previous studies provided abundant evidence related to the inter-annual variability of LST in urban areas for a better understanding of the driving mechanisms of the urban thermal environment. For

instance, Xiang et al. (2021) showed that landscape composition, biophysical parameters, and climate conditions during seasons lead to an inter-seasonal variation of LST in an urban agglomeration, China. However, the effect of urbanization on urban inter-annual (temporal) LST variability (ALSTV) is still unclear and poorly understood due to the multitude of influential factors such as the spatial pattern of the urban landscape. ALSTV, in this research, is defined as the difference between the annual minimum and maximum temperature that can be achieved using LST. Many studies in this area have shown that urban expansion influences seasonal and annual LST but this effect may vary depending on the geographical, topographical, and spatial pattern characteristics of the study region, which requires region-specific studies in the field of urban expansion and LST variability (Zhou et al. 2016; Li et al 2022).

In this research, we focused on urban inter-annual temperature to investigate how urban growth results in increased ALSTV in a rapidly urbanizing and semi-arid region in the Karaj urban area, north of Iran. The study area of this research, experienced an unplanned and accelerated urban expansion in the past decades (Taleshi and Ghobadi, 2012), replacing vegetation cover with built-up areas that lead to creating UHIs (Mokhtari et al, 2022). Considering the above background, in this research, to investigate the effect of urban expansion on the Karaj UHI and its thermal consequences, a hierarchical LULC classification approach was adopted. At first, Sentinel-2 image segmentation was performed to identify homogeneous areas having the same interior LULC patterns. Then, patch-based built-up (residential) areas were extracted using a pixel-based classification procedure and applied for the calculation of their spatial patterns. Relying on the ability of the Google Earth Engine, ALSTV was estimated using two temporally-median-filtered Landsat-8 TIRS images. The multiple linear regression model was applied to investigate how the ALSTV of built-up patches can be explained by their spatial patterns and those of surrounding

patches situated within the same spectral segment. Ultimately, the current urban area was modeled to grow up to 5% of the study region using a spatially-informed CA model that can identify the urban patches that will experience an increased ALSTV in the future.

Material and methods

Study area

The study area of this research includes Karaj (capital of Alborz Province), Shahriar and Mohammad-Shahr cities and their surrounding suburbs. The area of the region is about 30818 ha, of which 7000 ha is administered by municipal authorities. The population of the Karaj region increased exponentially more than seventy times in the last five decades (1967-2017). Due to its proximity to the capital and favorable weather, after Tehran, Karaj is the largest immigrant-friendly city in Iran (https://karaj.ir). With over 2.2 million inhabitants, it is the fourth-most populous urban district in the country (https://www.amar.org.ir). Topographically, the area is 1300 m above sea level and has plain land, sloping gently (less than 3%) from northeast to southwest. The climate of the study area is a four-season arid and semi-arid according to De Martonne's climatic classification scheme (https://www.amar.org.ir). The vegetation cover of the Karaj urban region includes public parks, planted tree-cover areas, fragmented croplands, and sparse rangeland (Mokhtari et al. 2021). The mean annual precipitation and temperature of the region are 247 mm and 14.4 °C. The hot season lasts from June to September. The hottest month of the year in Karaj is July with a mean temperature of 34.6 °C. The cold season lasts from November the March and the coldest month is February with a mean temperature of 9.2 °C (https://alborz.mporg.ir). Notably, over the past decades, this area has experienced warmer summers and a high rate of heat-related mortality (Ghobadi et al, 2018). Fig. 1 shows the study area of the present research.

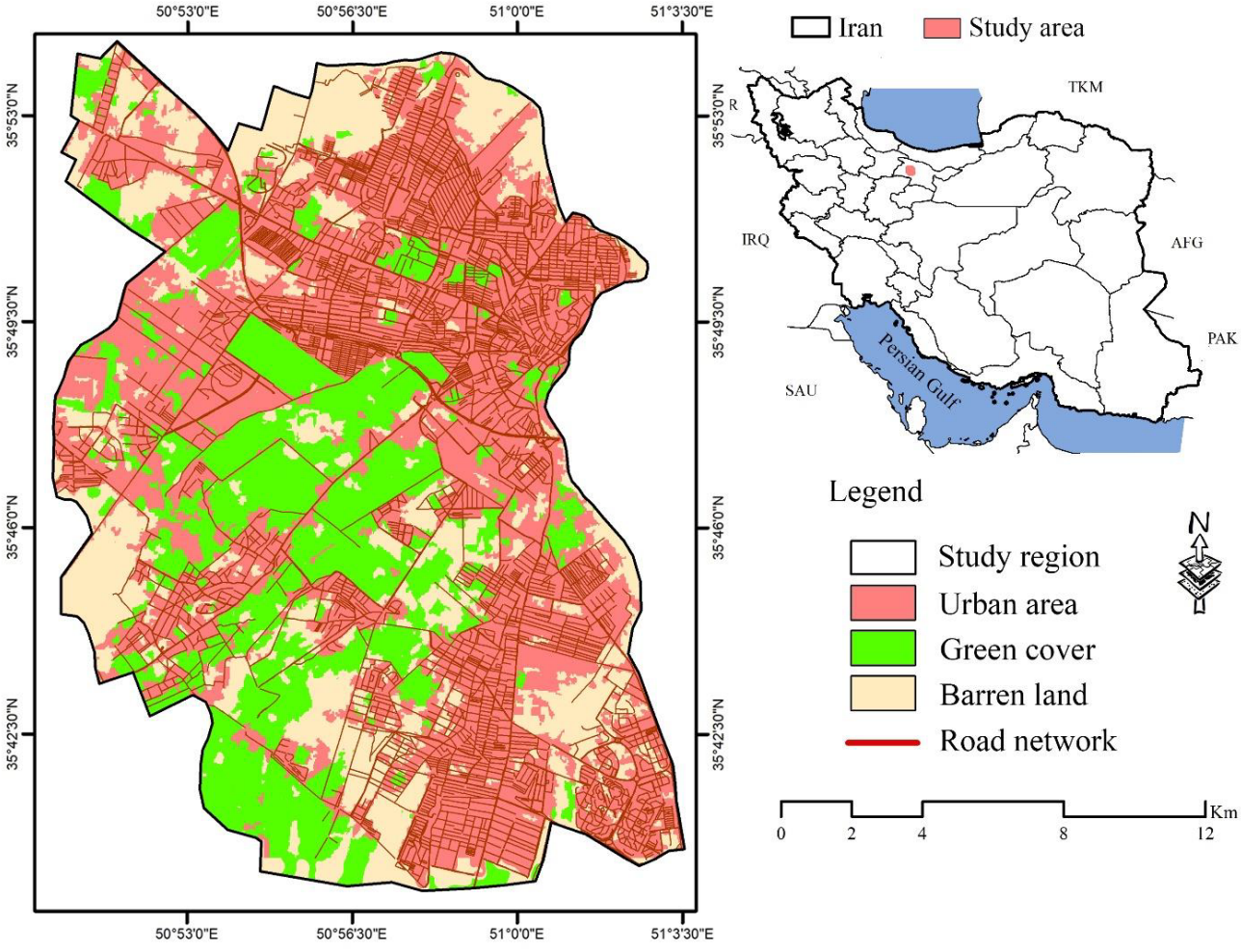


Fig. 1. Location of the study area

LST and LULC generation

To retrieve the ALSTV layer, we used the Landsat 8- Thermal Infrared Sensor (TIRS) images taken in 2021, except for those images that were covered by clouds and other atmospheric disturbances. Moreover, images taken three days after heavy rains were excluded as they might not represent an actual estimate of the region's LST. Excluding these dates, all of the 2021 Landsat 8-TIRS band 10 images were selected from the open-source Google Earth Engine platform (Mutanga and Kumar 2019). Then, two combined band 10 images were created by applying the maximum and minimum filters. LST retrieval from band 10 has higher accuracy than band 11

because of TIRS calibration issues (Yu et al., 2014). The maximum-radiated band 10 was created using the pixels of eight images taken on hot summer days while the minimum-radiated band 10 was created using seven images of cold winter days. Both images were processed using the Radiative Transfer Equation-based method to retrieve LST values (Ezimand et al. 2021). At first, the sensor-specific gain and offset coefficients were used to convert the image raw values (Digital Numbers- *DN*) to spectral radiance using **Eq. 1**, followed by conversion to at-satellite brightness temperature (*T*) using **Eq. 2** where k1 and k2 are band-specific thermal conversion constants, which are 774.89 and 1321.08, respectively (Cristóbal et al. 2018). The land surface emissivity was calculated using the Landsat-8 band 10 based on the NDVI proposed by Sobrino et al. (2008). LST were calculated using **Eq. 3**, where λ represents emitted wavelength, α is Boltzman constant (1.38*10−23 k/J), h is Plank constant (6.626×10−34 J/s); c is the light velocity (2.998×108 m/s), and ε is the emissivity of the land surface.

$$L(\lambda) = gain\ (DN) + offset \qquad \text{Eq. 1}$$

$$T = K_2 / \ln\left(\frac{K_1}{L(\lambda)} + 1\right) - 272.15 \qquad \text{Eq. 2}$$

$$LST = T/[1 + (\lambda \times \mathrm{T}/(\mathrm{h} \times \mathrm{c}/\alpha) \ln \varepsilon \qquad \text{Eq. 3}$$

The LULC layer of the region was created using a median-filtered image produced from the Sentinel-2 taken over the year 2021 into three classes built-up, green cover, and bare land. In doing so, the maximum likelihood classifier was trained using 70% of reference data collected through random visual inspection of aerial photographs. Using the remaining 30% (total of 500 reference points), the error matrix was constructed to assess the validity of image classification, assuming that user and producer accuracies (Comber, 2013) of more than 80% indicate an acceptable classification performance. User accuracy is calculated for each class to assess that how much a class belong to that class on the ground. Producer accuracy calculation for each class indicates

how well the classification was performed (i.e. without addressing their actual situation on the ground) (Enderle & Weih Jr, 2005).

Quantifying independent variables

Drawing from the literature review and experts' opinions with the exception of significantly correlated variables, a set of structural and neighborhood factors were measured to construct an ALSTV predictive model for built-up patches. Structural variables included the area, shape index (SI), and core area (CORE) of built-up patches calculated at the patch level using the FRAGSTATS landscape pattern analysis program (McGarigal, 2006). SI refers to the complexity of a patch shape while CORE refers to the interior patch area (Table 1) (McGarigal, 1995). In this research, neighborhood-independent variables were measured within a spectral segment generated from the Sentinel-2 image. The segments were generated using the multi-resolution segmentation method (Li et al., 2021). This method requires the setting of four major parameters including scale, band weight, compactness, and shape. As suggested by H. Tong, Maxwell, Zhang, and Dey (2012), the values of these parameters were set through trial and error until achieving a satisfactory segmentation with scale, compactness, and shape values of 50, 0.3, and 0.5 and equal band weights of 1. Mean patch size (MPS), percentage of built-up and green land cover (B-PLAND and G-PLAND, respectively), number of built-up patches (NP) and their mean distance from each other (Euclidian Near Neighbor- ENN), and Shannon Evenness index (SHEI) of LULC classes were calculated within each segment as neighborhood variables affecting the segment overall ALSTV and their built-up patches. A brief description of the spatial metrics used to measure neighborhood variables is given in Table 1 (McGarigal, 1995).

Table 1. The equation, variable description, and range of spatial metrics used to predict built-up ALSTV

Metric	Formula	Variable description	Range (unit)
NP	$NP = n_i$	n is the total number of patches	NP ≥ 1
PLAND	$PLAND = \frac{\sum_{j=1}^{n_i} a_{ij}}{A} (100)$	a_{ij} is an area (m^2) of patch ij A is total landscape area (m^2)	0 < PLAND ≤ 100
MPS	$MPS = \frac{1}{n_i} \sum_{j=1}^{n_i} a_{ij}$	n is the total number of patches a_{ij} is an area (m^2) of patch ij	MPS ≥ 0 (ha)
CORE	$CORE = a_{ij}^{c} (\frac{1}{10000})$	a_{ij}^{c} is the area within a patch that is farther than a distance from the patch edge	CORE ≥ 0 (ha)
SI	$SI = p_{ij}/2\sqrt{\pi a_{ij}}$	a_{ij} is an area (m^2) of patch ij p_{ij} is perimeter (m) of patch ij	SI ≥ 1
ENN	$ENN = \sum_{j=1}^{n_i} h_{ij} / n_i$	Distance (m) from patch ij to nearest neighboring patch n is the total number of patches	ENN > (m)
SHEI	$SHEI = \frac{-\sum_{i=1}^{m} (p_i - \ln p_i)}{\ln m}$	p_i is the proportion of the landscape occupied by patch type i m is the number of patch types	0 ≤ SHEI ≤ 1

The multiple linear regression model (Hu et al., 2019) between ALSTV layer as the dependent variable and a set of structural and neighborhood variables was used to construct a predictive model of ALSTV for each built-up patch and the segments. Due to the careful selection of independent variables, the collinearity among them was expected to be minimal; however, the Variance Inflation Factor (VIF) (Vörösmarty & Dobos, 2020) was used for collinearity diagnosis, considering that a model with a VIF value of more than 3 is subject to collinearity. The non-normal distribution of independent variables was normalized using the Box-Cox transformation technique (Begum & Dohi, 2018). Finally, the best-fit regression model was chosen based on the highest coefficient of determination (R^2).

Future urban growth scenario

To suggest a practical implementation of the model, we applied an informed urban growth procedure to simulate future urban expansion at a time t when built-up areas would grow up to 5 % of the region's area. To do so, we used a Cellular Automata (CA) (X. Tong & Feng, 2020) model for 5% allocation of the area to new urban pixels. The allocation process was guided using an urban suitability map produced by the multi-criteria evaluation (MCE) method (Meena, Mishra, & Tavakkoli Piralilou, 2019). Nine factor layers including slope, land use, and distance from the highway, rail transport, primary and secondary roads, urban centers commercial facilities, and recreational attractions were chosen and fuzzified using different membership functions as given in Table 2. Constraint boolean-derived layers indicating zero potential for conversion to built-up area consisted of built-up mapped in 2020, transportation network, urban parks, and river and stream network. The relative importance of factor layers was determined using the analytic hierarchy process (AHP) (Teknomo, 2006) and judgments of local experts' opinions. The fuzzified and relatively weighted factor layers together with constraints were integrated linearly using the weighted linear combination (WLC) (Eq. 4) where W_i is the relative weight of factor i (X_i) and C is constraints.

$$WLC = \sum_{i=1}^{n}(W_i \times X_i) \prod C \qquad \text{Eq. 4}$$

The regression model was finally used to predict the ALSTV of every single built-up patch at time t using their area, MPS, ENN, and B-PLAND of their corresponding segment assuming that green cover areas (including agricultural and planted tree-cover areas) would not change to bare land. In other words, the spatial characteristics of every single built-up patch were calculated and implemented in the best-fit regression model to estimate their ALSTV. The steps undertaken in this research are represented in Fig. 2.

Table 2. Factor and constraint layers, fuzzification parameters and the results of AHP prioritization used for urban suitability mapping

	Criteria	Fuzzy membership function	Control points				AHP priority
			a	b	c	d	
Factor	Slope (degree)	D.S*	-	-	6	12	0.103
	Land use	Rating	Bareland (1.0), Agriculture (0.7), Urban green area (0.1)				0.236
	Highway (m)	U.D*	0	1000	3000	5000	0.054
	Rail transport (m)	U.D*	0	2000	3000	6000	0031
	Primary road (m)	D.J*	-	-	0	2000	0.221
	Secondary road (m)	D.L*	-	-	0	1000	0.066
	Urban center (m)	D.L	-	-	0	6000	0.141
	Commercial facilities (m)	D.L	-	-	0	5000	0.065
	Recreational attractions (m)	D.L	-	-	0	5000	0.082
	Consistency ratio						6.2 %

*D is Decreasing form, U is User-defined form, S is Sigmoidal type, J is J-shape type, and L is Linear type

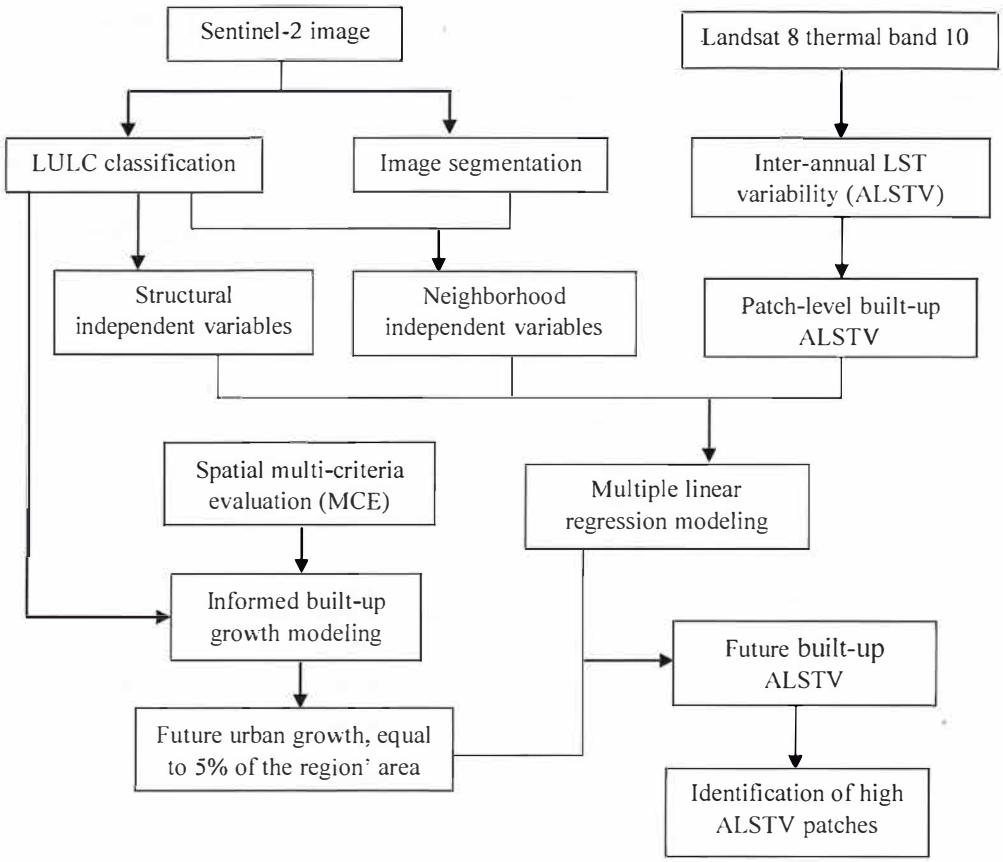


Fig. 2. Research flowchart

Results

The Landsat 8-based inter-annual variability of LST was created for 2021 (Fig. 3). The lowest ALSTV was found to be 19.05 °C. The mean ALSTV was highest in urban areas (33.25± 7.41 °C), while the lowest mean value of 24.12± 3.24 was observed in green covers (Table 3). Spatially, ALSTV was highest in northern parts of the region where urban areas are relatively compact with homogeneous built-up surfaces (higher B-PLAND and B-MPS and lower B-ENN) **(Fig. 3).** The accuracy of Sentinel-2 image classification was found to be satisfactory such that both user and producer accuracies were above 80% (Table 3). Particularly, the user and producer accuracies of urban areas were 87.05 and 95.75 %, respectively, indicating that approximately 20.7 % (6396.31 ha) of the region is covered by built-up areas. The results of multi-resolution segmentation are

shown in Fig. 3. In total, 865 segments were created. The smallest segment with an area of 1.25 ha was related to a dense tree cover while the largest segment of 387.43 ha belonged to a homogenous bare land in the southwest of the region (Table 4). On average, segments had an area of 35.62 ha with a high standard deviation (36.74), which demonstrates high heterogeneity of landscape characteristics in the study area.

Table 3. Annual LST variability, area, and accuracy results of LULC classes

Statistics		LULC		
		Urban area	Green cover	Bare land
ALSTV	Mean	33.25	24.12	26.18
	Stdev.	7.41	3.24	4.87
# of reference points		330	178	131
User accuracy		87.05	97.26	80.76
Producer accuracy		95.75	79.77	80.15
Area (ha)		6396.31	5942.01	18480.23

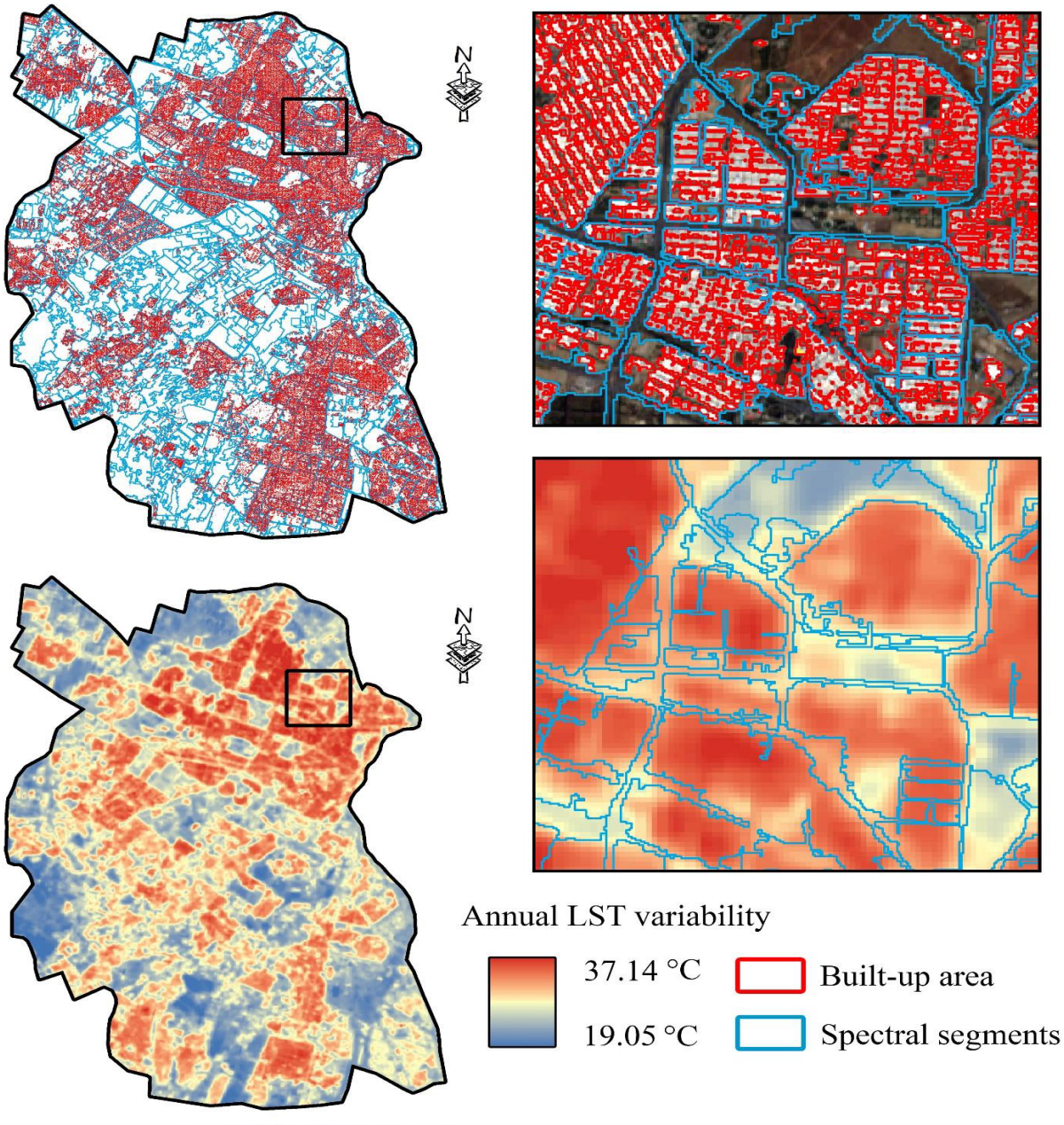


Fig. 3. Layers of annual LST variability, built-up areas, and spectral segments derived from Landsat-8 and Sentinel-2 images

The area of built-up patches ranged from 0.01 (equal to Sentinel-2 pixel size) to 29.56 ha with a mean of 3.84± 6.43 ha (Table 4). The mean SI of built-up patches was 1.51± 0.49. Small built-up

patches, particularly single-pixel ones had no core area, whereas the largest built-up patch of the study area had a core of 18.85 ha. The mean core size of built-up patches was 9.34± 7.43 ha (Table 4). The number of within-segment built-up patches ranged from 0 (in 21 segments) to over 430 (mean of 54.16± 94.34). In compact segments, B-ENN values were 22 m. However, in the center and southwest of the area where the sprawl growth pattern is dominant, the class-level B-ENN values increased to more than 500 m (Table 4). The mean size of built-up patches within the spectral segments was found to be 16.57± 20.67 ha in a range of 46.42 ha. The most built-up dominated segment had a B-PLAND of more than 94. Moreover, less than 20% of the segments' area was occupied by green structures. The SHEI index ranged between 0.01 and 0.69 with a mean value of 0.34± 0.17 (Table 4).

Table 4. Statistics of spectral segments, urban patch structure, and neighborhood variables

Variable		Statistics			
		Min.	Max.	Mean	Stdev.
Segment	Area	1.25	387.43	35.62	36.74
Built-up patch structure	Area	0.01	29.56	3.84	6.43
	Core	0.00	18.85	9.34	7.43
	SI	1.13	1.22	1.51	0.49
Neighborhood	B-NP	0	433	54.16	94.34
	B-PLAND	0.00	94.18	48.53	33.76
	G-PLAND	0.00	83.24	19.54	16.43
	B-MPS	0.00	46.42	16.57	20.67
	B-ENN	22.24	539.22	135.61	109.43
	SHEI	0.01	0.69	0.34	0.17

Although there was no significant correlation ($p > 0.01$) between the selected variables, they all had non-normal distributions either due to excessive skewness or kurtosis. The Box-Cox transformation was used to convert independent variables to normal distributions with p-values between 0.157 and 0.200. The best-fit ALSTV regression model was built with $R^2 = 0.637$ ($p =$

0.000) using four independent variables of built-up patch area (t = 1.615, p = 0.000) (Eq. 5), B-MPS (t= 2.773, p = 0.002), B-PLAND (t = 1.269, p = 0.004) and G-PLAND (t = -2.108, p = 0.043) (Table 5). Due to the participation of non-correlated independent variables, all VIF values showed an acceptable range of 1.223 (Area) to 2.625 (G-PLAND), resulting in an interpretable regression model. Except for G-PLAND, other variables had a positive contribution to ALSTV, indicating that increasing ALSTV of a built-up patch is a function of its area and the percentage and size of those built-up patches creating a spectral segment. Moreover, increasing percentag of green cover within a segment would alleviate ALSTV.

$$Annual\ LST\ variability = 12.552 + 2.286\,(\text{Area}) + 1.475(\text{B} - \text{MPS}) + 1.007\,(\text{B} - \text{PLAND}) - 0.349\,(\text{G} - \text{PLAND}) + \varepsilon \quad \text{Eq. 5}$$

Table 5. Statistics of the best-fit multiple linear regression model and results of collinearity diagnostics

Model	Unstandardized Coefficients		Standardized Coefficients	t	Sig.	Collinearity	
	B	Std. Error	Beta			Tolerance	VIF
(Constant)	12.552	7.976		4.690	0.010		
Area	2.286	1.416	0.297	1.615	0.000	0.818	1.223
B-MPS	1.475	0. 532	0.301	2.773	0.002	0.764	1.308
B-PLAND	1.007	0.793	1.336	1.269	0.004	0.463	2.160
G-PLAND	-0.349	0.165	-0.183	-2.108	0.043	0.381	2.625

The urban growth suitability map of the region was driven by multi criteria evaluation (MCE), which is illustrated in Fig. 4 A. The highest urban growth suitability was found to be within dense urban patches in urban centers and near commercial and recreational hotspots. The effect of the road network was more important in central and southwestern parts of the region, where scattered urban growth is more prominent. The CA-resulting 5% future urban growth is shown in Fig. 4. Approximately, all of the future urban growth, accounting for 1588.64 ha, was projected to occur in edge-growth and in-fill patterns such that larger patches became bigger, while small urban

patches experienced a relatively low area growth due to the low suitability of land in areas with sprawling development pattern. As shown in Fig. 4 B, some parts of the region are likely to experience in-fill growth patterns, which may face increased ALSTV or increased segment ALSTV. Using Eq. 5, the ALSTV of every built-up patch and segment was calculated. The projected ALSTV of simulated built-up patches is represented in Fig. 4 C. Patches that will experience ALSTV of more than 40 °C are colored in dark blue, accounting for an area of around 1475.47 ha. As shown in this figure, patches with high ALSTV values were distributed dispersedly across the region in areas expected to experience notable future urban growth.

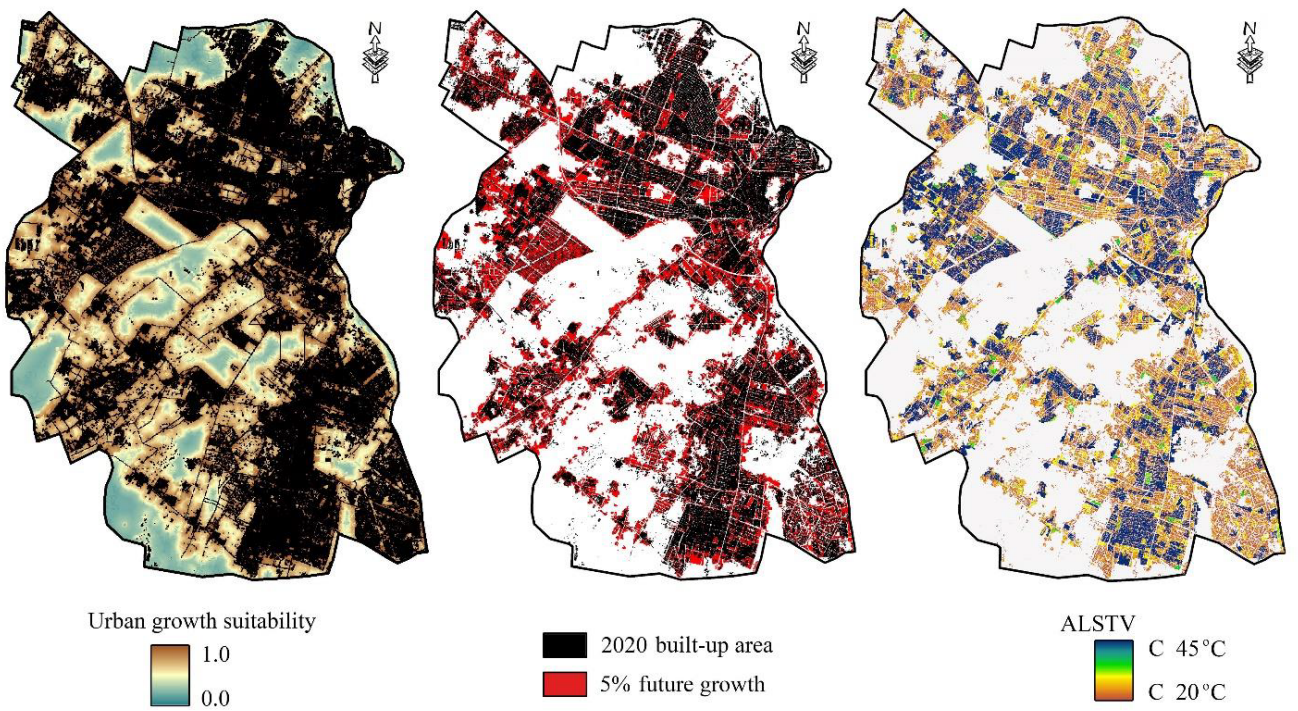


Fig. 4. A: Spatial distribution of urban growth suitability; B: Future 5% growth simulation; C: ALSTV of the simulated built-up patches.

Discussion

The results of the research showed that built-up class faced the most extreme temperature changes in urban areas (33.25± 7.41 °C), while the lowest mean value of 24.12± 3.24 was observed in green covers. Moreover, the ALSTV of built-up patches showed a positive relationship with their area

and the percentage and size of neighborhood built-up patches while negatively related with the percentage of neighborhood green patches. Drawing from the results, the ALSTV range is positively associated with the area of built-up patches (compositional characteristics) irrespective of their spatial structure and landscape configuration.

Methodologically, in this research, to construct a better ALSTV predictive model, neighborhood (spatial) factors were taken into account. A wide source of evidence indicates that the thermal characteristics of LULC patches not only are a function of their spatial pattern but also are affected by neighborhood factors. Hence, some urban planning strategies took advantage of green covers' cooling capacity to mitigate built-up LSTs in neighboring areas (Asgarian, Amiri, & Sakieh, 2015; Rouhi, Chamani, Jafarnezhad, & Asgarian, 2018). In studies focusing on the spatial effects of adjacent factors, neighborhood variables are usually measured within a series of buffer rings around the predicting variable of interest (Connors, Galletti, & Chow, 2013; Gage & Cooper, 2017; Rouhi et al., 2018). Putting them together, to explore neighborhood effects, different procedures have been adopted in the literature: using radius distances (F. Liu, Jia, Li, Du, & Wang, 2020; White-Newsome et al., 2013), edge boundaries (Chen, Zhou, Man, & Liu, 2021; Chun & Guldmann, 2014), and moving window method (Meng et al, 2022). In this study, a new approach to investigate neighborhood effects was introduced based on spectral characteristics. In such a way that neighborhood independent variables were measured within a network of spectral segments computed from the Sentinel-2 image applied for LULC classification. Although the segmentation process was performed on spectral bands, its validation was carried out by visual-spatial matching of the segments with the ALSTV layer. Moreover, we assumed that if the segments are a reliable measure of the neighborhood, some LULC characteristics of the segments could be incorporated into developing the best patch-level ALSTV predictive model.

The findings indicated that the ALSTV of urban patches is also affected by neighborhood built-up and green patches (Table 5). The ALSTV of patches is expected to be high in segments that are highly dominated by large-sized built-up patches (higher B-PLAND and B-MPS values). In other words, segments with higher ALSTV values might induce higher thermal variability in the newly-developed urban patches. In line with our results, H. Liu and Weng (2008) and Zhang, Odeh, and Ramadan (2013) also found that the mean size of urban patches in newly developed zones is high and exhibits relatively higher mean LST values. In this research, a meaningful negative relationship was found between the ALSTV of urban patches and the percentage of their respective segments covered by green areas. This is consistent with the results of numerous studies related to the cooling effect of urban green areas (Hamada & Ohta, 2010; C. Wu et al., 2021; B. Zhang, Gao, & Yang, 2014; Das, Das, & Momin, 2022).

The results of the best-fit regression model showed that the area of built-up patches is the most important explanatory variable of ALSTV such that larger urban patches might experience higher degrees of temperature in summer while lower degrees in winter. In some Iranian landscapes, the area of built-up patches was also identified as the single most important variable explaining spatio-temporal variations in LST (Afrakhteh, Asgarian, Sakieh, & Soffianian, 2016). Based on the results, it seems that the ALSTV range is positively associated with the area of built-up patches irrespective of their spatial structure and landscape configuration.

Related to the projected urban growth of the study area, the results of urban expansion modeling showed that the region has a high tendency to become more compact through filling inter-urban vacant areas, which are seen throughout the study area, thus adversely affecting the region's thermal environment. This is in agreement with previous findings (Fu & Weng, 2018; Harrison &

Winfree, 2015), which indicate that compact urban areas experienced high ALSTV (S. Zhao, Liu, & Zhou, 2016).

This result has profound implications for urban landscape planning, indicating that segment-based urban greening may be more effective in areas suffering from high ALSTV. Similar to our findings, Wu, Yao, and Ren (2020) found that the spatial variation of LST can be statistically better explained, predicted, and exploited for management when the urban complex landscape is divided into functionally heterogeneous zones.

In this study, we considered urban green patches, urban segments, and the effect of climate change as constant to predict the future ALSTV of urban patches. Due to adopting a segment-based approach, ALSTV was found to be more sensitive to the local growth of individual urban patches and their adjacent LULCs. This finding urges a shift in the focus of urban policies from high-growth areas to all areas in order to form new urban clusters. According to our results, further allocation of green patches (such as urban parks) and preventing the excessive growth of urban patches are essential in all large built-up segments across the entire study area to create a thermally-comfortable landscape.

Conclusion

This study developed an integrated modeling approach to estimate the future annual variability of the LST in Karaj urban area as a rapidly urbanizing and semi-arid in Iran. The results showed that the highest ALSTV was in built-up areas while the lowest value was observed in the green area. The ALSTV of built-up was positively associated with their area and the percentage and size of neighborhood built-up patches whereas neighborhood green patches decreased ALSTV. The results also indicated that the size of built-up patches is the primary factor in the variability of urban LST. Moreover, the results highlighted the importance of both local and neighborhood

effects of LULC classes on ALSTV in semi-arid urban areas. The research findings indicate that the urban surface thermal sources can be identified, modeled, and predicted using the local (segment-based) LULC characteristics. Due to the importance of the LULC neighborhood factors, it is suggested to employ LULC change modeling techniques to investigate the spatial dynamics of all LULCs, especially green covers, and simulate the spatial dynamics of spectral segments using the predicted LULC maps. Overall, this study can provide new insight to optimize landscape planning for achieving sustainable development.

References

Achmad, A., Fadhly, N., Deli, A., & Ramli, I. (2022). Urban growth and its impact on land surface temperature in an industrial city in Aceh, Indonesia. *Letters in Spatial and Resource Sciences*, 1-20.

Afrakhteh, R., Asgarian, A., Sakieh, Y., & Soffianian, A. (2016). Evaluating the strategy of integrated urban-rural planning system and analyzing its effects on land surface temperature in a rapidly developing region. *Habitat International, 56*, 147-156.

Allen, M. A., Roberts, D. A., & McFadden, J. P. (2021). Reduced urban green cover and daytime cooling capacity during the 2012–2016 California drought. *Urban Climate, 36*, 100768.

Asgarian, A., Amiri, B. J., & Sakieh, Y. (2015). Assessing the effect of green cover spatial patterns on urban land surface temperature using landscape metrics approach. *Urban Ecosystems, 18*(1), 209-222.

Asgarian, A., Soffianian, A., Pourmanafi, S., & Bodaghabad, M. B. (2018). Evaluating the spatial effectiveness of alternative urban growth scenarios in protecting cropland resources: A case of mixed agricultural-urbanized landscape in central Iran. *Sustainable Cities and Society, 43*, 197-207.

Avdan, U., & Jovanovska, G. (2016). Algorithm for automated mapping of land surface temperature using LANDSAT 8 satellite data. *Journal of sensors, 2016*.

Azhdari, A., Soltani, A., & Alidadi, M. (2018). Urban morphology and landscape structure effect on land surface temperature: Evidence from Shiraz, a semi-arid city. *Sustainable Cities and Society, 41*, 853-864.

Begum, M., & Dohi, T. (2018). Optimal release time estimation of software system using Box-Cox transformation and neural network. *International Journal of Mathematical, Engineering and Management Sciences, 3*(2), 177.

Bozorgi, M., Nejadkoorki, F., & Mousavi, M. B. (2018). Land surface temperature estimating in urbanized landscapes using artificial neural networks. *Environmental Monitoring and Assessment, 190*(4), 1-10.

Chen, L., Zhou, B., Man, W., & Liu, M. (2021). Landsat-Based Monitoring of the Heat Effects of Urbanization Directions and Types in Hangzhou City from 2000 to 2020. *Remote Sensing, 13*(21), 4268.

Chun, B., & Guldmann, J.-M. (2014). Spatial statistical analysis and simulation of the urban heat island in high-density central cities. *Landscape and Urban Planning, 125*, 76-88.

Comber, A. J. (2013). Geographically weighted methods for estimating local surfaces of overall, user and producer accuracies. *Remote Sensing Letters, 4*(4), 373-380.

Connors, J. P., Galletti, C. S., & Chow, W. T. (2013). Landscape configuration and urban heat island effects: assessing the relationship between landscape characteristics and land surface temperature in Phoenix, Arizona. *Landscape ecology, 28*(2), 271-283.

Cristóbal, J., Jiménez-Muñoz, J. C., Prakash, A., Mattar, C., Skoković, D., & Sobrino, J. A. (2018). An improved single-channel method to retrieve land surface temperature from the Landsat-8 thermal band. *Remote Sensing, 10*(3), 431.

Das, M., Das, A., & Momin, S. (2022). Quantifying the cooling effect of urban green space: A case from urban parks in a tropical mega metropolitan area (India). *Sustainable Cities and Society, 87*, 104062.

Effati, F. (2022). Landscape Metrics as Tool for Investigating the Relationship between Landscape Patterns and Land Surface Temperature in suitable scale (Case Study: Tehran City. *Journal of Environmental Science and Technology*.

Enderle, D. I., & Weih Jr, R. C. (2005). Integrating supervised and unsupervised classification methods to develop a more accurate land cover classification. *Journal of the Arkansas Academy of Science, 59*(1), 65-73.

Ezimand, K., Chahardoli, M., Azadbakht, M., & Matkan, A. A. (2021). Spatiotemporal analysis of land surface temperature using multi-temporal and multi-sensor image fusion techniques. *Sustainable Cities and Society, 64*, 102508.

Feng, L., Zhao, M., Zhou, Y., Zhu, L., & Tian, H. (2020). The seasonal and annual impacts of landscape patterns on the urban thermal comfort using Landsat. *Ecological Indicators, 110*, 105798.

Fu, P., & Weng, Q. (2018). Variability in annual temperature cycle in the urban areas of the United States as revealed by MODIS imagery. *ISPRS journal of photogrammetry and remote sensing, 146*, 65-73.

Gage, E. A., & Cooper, D. J. (2017). Relationships between landscape pattern metrics, vertical structure and surface urban Heat Island formation in a Colorado suburb. *Urban Ecosystems, 20*(6), 1229-1238.

Gao, S., Zhan, Q., Yang, C., & Liu, H. (2020). The diversified impacts of urban morphology on land surface temperature among urban functional zones. *International Journal of Environmental Research and Public Health, 17*(24), 9578.

Gerhards, M., Schlerf, M., Mallick, K., & Udelhoven, T. (2019). Challenges and future perspectives of multi-/Hyperspectral thermal infrared remote sensing for crop water-stress detection: A review. *Remote Sensing, 11*(10), 1240.

Ghobadi, A., Khosravi, M., & Tavousi, T. (2018). Surveying of heat waves impact on the urban heat islands: Case study, the Karaj City in Iran. *Urban Climate, 24*, 600-615.

Han, G., Chen, H., Yuan, L., Cai, Y., & Han, M. Field measurements on micro-climate and cooling effect of river wind on urban blocks in Wuhan city. In *2011 International Conference on Multimedia Technology, 2011* (pp. 4446-4449): IEEE

Hamada, S., & Ohta, T. (2010). Seasonal variations in the cooling effect of urban green areas on surrounding urban areas. *Urban forestry & urban greening, 9*(1), 15-24.

Harrison, T., & Winfree, R. (2015). Urban drivers of plant- pollinator interactions. *Functional Ecology, 29*(7), 879-888.

Hu, Y., Yu, S., Qi, X., Zheng, W., Wang, Q., & Yao, H. (2019). An overview of multiple linear regression model and its application. *Zhonghua yu Fang yi xue za zhi [Chinese Journal of Preventive Medicine], 53*(6), 653-656.

Khan, M., Tahir, A. A., Ullah, S., Khan, R., Ahmad, K., Shahid, S. U., et al. (2022). Trends and projections of land use land cover and land surface temperature using an integrated weighted evidence-cellular automata (WE-CA) model. *Environmental Monitoring and Assessment, 194*(2), 1-16.

Kowe, P., Mutanga, O., Odindi, J., & Dube, T. (2021). Effect of landscape pattern and spatial configuration of vegetation patches on urban warming and cooling in Harare metropolitan city, Zimbabwe. *GIScience & Remote Sensing, 58*(2), 261-280.

Kumar, D. (2015). Remote sensing based vegetation indices analysis to improve water resources management in urban environment. *Aquatic Procedia, 4*, 1374-1380.

Lakra, K., & Sharma, D. (2019). Geospatial assessment of urban growth dynamics and land surface temperature in Ajmer Region, India. *Journal of the Indian Society of Remote Sensing, 47*(6), 1073-1089.

Li, Y., He, J., Chen, F., Han, Z., Wang, W., Chen, G., et al. (2021). Generation of Homogeneous Slope Units Using a Novel Object-Oriented Multi-Resolution Segmentation Method. *Water, 13*(23), 3422.

Liu, F., Jia, X., Li, W., Du, A., & Wang, D. (2020). Analysis of land surface temperature evolution based on regional road scope. *Advances in Civil Engineering, 2020*.

Liu, H., & Weng, Q. (2008). Seasonal variations in the relationship between landscape pattern and land surface temperature in Indianapolis, USA. *Environmental Monitoring and Assessment, 144*(1), 199-219.

Liu, Y., Peng, J., & Wang, Y. (2018). Efficiency of landscape metrics characterizing urban land surface temperature. *Landscape and Urban Planning, 180*, 36-53.

Madanian, M., Soffianian, A. R., Koupai, S. S., Pourmanafi, S., & Momeni, M. (2018). Analyzing the effects of urban expansion on land surface temperature patterns by landscape metrics: a case study of Isfahan city, Iran. *Environmental Monitoring and Assessment, 190*(4), 1-11.

McGarigal, K. (1995). *FRAGSTATS: spatial pattern analysis program for quantifying landscape structure* (Vol. 351): US Department of Agriculture, Forest Service, Pacific Northwest Research Station.

McGarigal, K. (2006). Landscape pattern metrics. *Encyclopedia of environmetrics*.

Meena, S. R., Mishra, B. K., & Tavakkoli Piralilou, S. (2019). A hybrid spatial multi-criteria evaluation method for mapping landslide susceptible areas in kullu valley, himalayas. *Geosciences, 9*(4), 156.mo

Meng, Q., Liu, W., Zhang, L., Allam, M., Bi, Y., Hu, X., ... & Jancsó, T. (2022). Relationships between Land Surface Temperatures and Neighboring Environment in Highly Urbanized Areas: Seasonal and Scale Effects Analyses of Beijing, China. *Remote Sensing*, *14*(17), 4340.

Mokhtari, Z., Barghjelveh, S., & Sayahnia, R. (2021). Heterogeneity of the thermal environment and its ecological evaluation in the urban region of Karaj. *Geography and Environmental Sustainability*, *11*(4), 37-58.

Mokhtari, Z., Barghjelveh, S., Sayahnia, R., Karami, P., Qureshi, S., & Russo, A. (2022). Spatial pattern of the green heat sink using patch-and network-based analysis: implication for urban temperature alleviation. *Sustainable Cities and Society*, 103964.

Muravyev, A. V. (2018). Geothermal monitoring as a way to predict volcanic eruptions and estimate geothermal energy resources. *Георесурсы, 20*(4 (eng)), 413-422.

Mutanga, O., & Kumar, L. (2019). Google earth engine applications. (Vol. 11, pp. 591): Multidisciplinary Digital Publishing Institute.

Qiu, K., & Jia, B. (2020). The roles of landscape both inside the park and the surroundings in park cooling effect. *Sustainable Cities and Society*, *52*, 101864.

Rahimi, E., Barghjelveh, S., & Dong, P. (2021). Quantifying how urban landscape heterogeneity affects land surface temperature at multiple scales. *Journal of Ecology and Environment, 45*(1), 1-13.

Rao, Y., Dai, J., Dai, D., & He, Q. (2021). Effect of urban growth pattern on land surface temperature in China: A multi-scale landscape analysis of 338 cities. *Land Use Policy, 103*, 105314.

Rehman, A., Qin, J., Pervez, A., Khan, M. S., Ullah, S., Ahmad, K., et al. (2022). Land-Use/Land Cover Changes Contribute to Land Surface Temperature: A Case Study of the Upper Indus Basin of Pakistan. *Sustainability, 14*(2), 934.

Ren, T., Zhou, W., & Wang, J. (2021). Beyond intensity of urban heat island effect: A continental scale analysis on land surface temperature in major Chinese cities. *Science of The Total Environment, 791*, 148334.

Rouhi, H., Chamani, N., Jafarnezhad, J., & Asgarian, A. (2018). Spatial assessment of the effects of in situ and neighbourhood factors on urban land surface temperature mitigation in a rapidly developing region. *International Journal of Urban Sustainable Development, 10*(3), 292-304.

Sakieh, Y., Jaafari, S., Ahmadi, M., & Danekar, A. (2017). Green and calm: Modeling the relationships between noise pollution propagation and spatial patterns of urban structures and green covers. *Urban Forestry & Urban Greening, 24*, 195-211.

Sakieh, Y., Salmanmahiny, A., Jafarnezhad, J., Mehri, A., Kamyab, H., & Galdavi, S. (2015). Evaluating the strategy of decentralized urban land-use planning in a developing region. *Land Use Policy, 48*, 534-551.

Sekertekin, A., & Bonafoni, S. (2020). Land surface temperature retrieval from Landsat 5, 7, and 8 over rural areas: Assessment of different retrieval algorithms and emissivity models and toolbox implementation. *Remote Sensing, 12*(2), 294.

Shojaei, M., Shayesteh, K., & Attaeian, B. (2019). The Effect of Landscape Pattern on Urban Temperature Changes in Hamadan. *Geography and Environmental Sustainability, 9*(3), 99-114.

Sobrino, J. A., Jiménez-Muñoz, J. C., Sòria, G., Romaguera, M., Guanter, L., Moreno, J., et al. (2008). Land surface emissivity retrieval from different VNIR and TIR sensors. *IEEE transactions on geoscience and remote sensing, 46*(2), 316-327.

Statistical Center of Iran (2016). Iran statistical yearbook. Management and Planning Organization Tehran.

Sun, X., Tan, X., Chen, K., Song, S., Zhu, X., & Hou, D. (2020). Quantifying landscape-metrics impacts on urban green-spaces and water-bodies cooling effect: The study of Nanjing, China. *Urban Forestry & Urban Greening, 55*, 126838.

Taleshi, M., & Ghobadi, A. (2012). Urban land use sustainability assessment through evaluation of compatibility matrix case study: Karaj City. *OIDA International Journal of Sustainable Development, 3*(1), 57-64.

Tang, Y., Lan, C., & Feng, H. (2018). Effect analysis of land-use pattern with landscape metrics on an urban heat island. *Journal of Applied Remote Sensing, 12*(2), 026004.

Teknomo, K. (2006). Analytic hierarchy process (AHP) tutorial. *Revoledu. com, 6*(4), 1-20.

Tong, H., Maxwell, T., Zhang, Y., & Dey, V. (2012). A supervised and fuzzy-based approach to determine optimal multi-resolution image segmentation parameters. *Photogrammetric Engineering & Remote Sensing, 78*(10), 1029-1044.

Tong, X., & Feng, Y. (2020). A review of assessment methods for cellular automata models of land-use change and urban growth. *International Journal of Geographical Information Science, 34*(5), 866-898.

Vörösmarty, G., & Dobos, I. Green purchasing frameworks considering firm size: a multicollinearity analysis using variance inflation factor. In *Supply Chain Forum: An International Journal, 2020* (Vol. 21, pp. 290-301, Vol. 4): Taylor & Francis

Wang, Y., Zhan, Q., & Ouyang, W. (2017). Impact of urban climate landscape patterns on land surface temperature in Wuhan, China. *Sustainability, 9*(10), 1700.

White-Newsome, J. L., Brines, S. J., Brown, D. G., Dvonch, J. T., Gronlund, C. J., Zhang, K., et al. (2013). Validating satellite-derived land surface temperature with in situ measurements: A public health perspective. *Environmental health perspectives, 121*(8), 925-931.

Wu, Z., Yao, L., & Ren, Y. (2020). Characterizing the spatial heterogeneity and controlling factors of land surface temperature clusters: A case study in Beijing. *Building and Environment, 169*, 106598.

Wu, C., Li, J., Wang, C., Song, C., Haase, D., Breuste, J., & Finka, M. (2021). Estimating the Cooling Effect of Pocket Green Space in High Density Urban Areas in Shanghai, China. *Frontiers in Environmental Science*, 181.

Xiang, Y., Huang, C., Huang, X., Zhou, Z., & Wang, X. (2021). Seasonal variations of the dominant factors for spatial heterogeneity and time inconsistency of land surface temperature in an urban agglomeration of central China. *Sustainable Cities and Society*, *75*, 103285.

Zhang, Y., Odeh, I. O., & Ramadan, E. (2013). Assessment of land surface temperature in relation to landscape metrics and fractional vegetation cover in an urban/peri-urban region using Landsat data. *International Journal of Remote Sensing, 34*(1), 168-189.

Zhang, B., Gao, J.-x., & Yang, Y. (2014). The cooling effect of urban green spaces as a contribution to energy-saving and emission-reduction: A case study in Beijing, China. *Building and environment, 76*, 37-43.

Zhao, H., Tan, J., Ren, Z., & Wang, Z. (2020). Spatiotemporal characteristics of urban surface temperature and its relationship with landscape metrics and vegetation cover in rapid urbanization region. *Complexity, 2020*.

Zhao, S., Liu, S., & Zhou, D. (2016). Prevalent vegetation growth enhancement in urban environment. *Proceedings of the National Academy of Sciences, 113*(22), 6313-6318.

Zhou, L., Hu, F., Wang, B., Wei, C., Sun, D., & Wang, S. (2022). Relationship between urban landscape structure and land surface temperature: spatial hierarchy and interaction effects. *Sustainable Cities and Society*, 103795.